Petroleum Science 23 (2026) 5972–5983

Contents lists available at ScienceDirect

Petroleum Science

journal homepage: www.keaipublishing.com/en/journals/petroleum-science

Original Paper

Bifunctional heterojunction catalyst adsorption-promoted catalytic oxidation of aromatic sulfides high-value conversion

Zhen-Dong Yu [a,1], Peng Cui [a,b,1], Kai-Kai Li [a], Su-Hang Xun [c,*], Hao-Feng Wu [a], Yi-Ru Zou [a], Xiao-Xiao Xing [d], Xiao-Xiao Yu [d], Pei-Wen Wu [a,b], Wen-Shuai Zhu [a,b,**]

[a] College of Chemical Engineering and Environment, State Key Laboratory of Heavy Oil Processing, China University of Petroleum (Beijing), Beijing, 102249, China
[b] School of Chemistry and Chemical Engineering, Jiangsu University, Zhenjiang, 212013, Jiangsu, China
[c] School of the Environment and Safety Engineering, Jiangsu University, Zhenjiang, 212013, Jiangsu, China
[d] State Key Laboratory of Heavy Oil Processing, College of Science, China University of Petroleum (Beijing), Beijing, 102249, China

ARTICLE INFO

Article history:
Received 30 July 2025
Received in revised form
11 January 2026
Accepted 6 April 2026
Available online 8 April 2026

Edited by Min Li

Keywords:
Heterostructure interface
Titanium dioxide
Adsorption-promoted oxidation
Oxidative desulfurization

ABSTRACT

With the increasing need for high-value utilization of diesel components, catalytic oxidative desulfurization (ODS) emerges as an efficient non-hydrogenation approach to desulfurization and utilization of aromatic sulfides. Although TiO_2 is a promising candidate for ODS, the catalytic activity is limited. Herein, with the heterojunction interface formation, a series of TiO_2/three-dimensional porous carbon nitride catalysts (Ti/3D g-C_3N_4) has been developed for ODS. Notably, the successful construction of the type II heterojunction between TiO_2 and 3D g-C_3N_4 is confirmed through systematic characterizations. The bandgap is narrowed in the hybrid materials, accelerating the electron transfer from the N to the Ti center, conducive to the activation of hydrogen peroxide in the radical pathway. Also, the emergence of micro-mesoporous pores in 3D g-C_3N_4 enhances the adsorption mass transfer of aromatic sulfides. The synergistic effect between heterostructures and extended mesopores generates superoxide radicals, attaining >99% adsorption-promoted catalytic oxidation reactivity of aromatic sulfides. The work develops bifunctional heterogeneous materials of efficient adsorption-promoted catalytic oxidation, expanding the development for the high-value utilization of sulfides in diesel fuel.

1. Introduction

The oil consumption in the primary energy structure of the world still takes the biggest part, about 33.6% in 2024, counted by the Energy Institute. With the continuous extraction of crude oil, the refining industry is facing increasingly heavy and inferior raw materials (Vogt and Weckhuysen, 2024). This means the energy consumption for processing crude oil is increased by a large margin. The processing of the crude oil involves atmospheric and vacuum distillation, catalytic cracking of heavy oil, catalytic hydrogenation and other processes (Davis et al., 2018). The diesel, as a part of petroleum processing products with a boiling point range from 180 to 410 °C, is composed of various types of chemical compounds. Among these compounds, alkanes, aromatic hydrocarbons, aromatic sulfides and aromatic nitrides are considered the main components (He et al., 2024; Yu et al., 2018). The efficient separation of different types of main components, in high-purity form at the molecular level, is conducive to achieving high-value utilization (C. Hu et al., 2024). Further, the separated components can be used as the raw materials for further production of optoelectronic materials (aromatic sulfides or sulfones), high-end carbon materials (aromatic hydrocarbons), etc (Liang et al., 2025; Liu et al., 2025; Xia et al., 2025).

Catalytic oxidative desulfurization technology (ODS) is an efficient non-hydrogenation strategy, which realizes the high-value utilization of aromatic sulfides under low energy consumption conditions (Wu et al., 2024). Usually at 25–150 °C, 1 atm, the aromatic sulfides can be converted into the sulfone compounds with higher polarity, which are prone to be separated from the less polar alkanes and aromatic components (Scheme 1).

* Corresponding author.
** Corresponding author.
E-mail addresses: xunsuhang@ujs.edu.cn (S.-H. Xun), zhuws@cup.edu.cn (W.-S. Zhu).
Peer review under the responsibility of China University of Petroleum (Beijing).
[1] These authors contributed equally to this work.

https://doi.org/10.1016/j.petsci.2026.04.005

Further coupling with the hydrogenation refining technology (or hydrodesulfurization, HDS) with ODS, directional resource recovery of dibenzothiophene sulfones ($DBTO_2$s) can be implemented (Wu et al., 2025). When the hydrogenation depth of catalytic diesel reaches the sulfide content below 2 wt%, mainly dibenzothiophenes (DBTs) and their homologues are enriched (Wang et al., 2024). The development of efficient and multifunctional catalysts, achieving catalytic oxidation of DBTs, is the key to high-value utilization of diesel.

Titanium dioxide (TiO_2) has been widely used in ODS because of its stability, low toxicity, wide availability and highly tunable properties (Ma et al., 2024; Yu et al., 2022; Zheng et al., 2025). However, when amorphous TiO_2 is used as a catalyst for ODS reaction, there are some unavoidable drawbacks, such as the limited specific surface area, barely exposed active sites, and poor dispersion in the oil phase (Liu et al., 2023; Tao et al., 2025; Yoon et al., 2025). To solve these problems, employing appropriate supports to improve the dispersibility of titanium-based materials is a promising strategy, where the interaction between the metal and the support is enhanced (Chen et al., 2025; Liu et al., 2025; Ye et al., 2025). This approach is expected to significantly improve the desulfurization rate. As a two-dimensional material, graphitic carbon nitride (g-C_3N_4) has been widely used in water photolysis for hydrogen production, electrocatalytic oxygen reduction, and solar cells (Li et al., 2026; Ye et al., 2025; Zeng et al., 2025). The attractiveness of this material lies in its diverse sources, ease of preparation, and high electronic conductivity. It has been reported that g-C_3N_4 can be used as a support to form heterojunctions with metallic oxides, inorganic carbon materials, and polymers (Lazaar et al., 2025). Porous modification of g-C_3N_4 is considered a promising approach to increase the specific surface area and improve the pore structure, thereby facilitating the movement of small molecule substrates during reactions (Dharmarajan et al., 2023). The porous g-C_3N_4 enables uniform distribution of the active components, and the unique triazine structure on its surface enhances the π-π and p-π adsorption with the DBT molecules, as well as the electron transfer effect of the central metal (D. Hu et al., 2024).

In this study, a series of bifunctional anatase TiO_2/three-dimensional porous carbon nitride catalysts are prepared for ODS reactions (Ti/3D g-C_3N_4). Through systemic characterization of high-resolution electron microscopy, EDX, Mapping, XPS and UV-DRS, etc., a type II heterojunction is successfully constructed after loading, narrowing the bandgap of Ti/3D g-C_3N_4. The crystal structure transformation of TiO_2 and the charge density on the surface of the skeleton N in 3D g-C_3N_4 have been studied in detail. Also, the specific surface area and dispersion of the active components are increased on the hybrid materials. In the adsorption-promoted catalytic oxidation process of Ti/3D g-C_3N_4, the resulting mesoporous structure of the three-dimensional lamellar stacking facilitates the enhancement of the adsorption capacity of DBT. The corresponding mechanism is investigated, and the electron-rich Ti center at the heterojunction interface can efficiently activate hydrogen peroxide. DBT is rapidly converted into sulfone by highly reactive $\cdot O_2^-$, which is demonstrated by the data of FT-IR and GC-MS. The conditional experiment is thoroughly examined, concerning the factors of reaction temperature, catalyst dosage and oxygen-sulfur ratio, as well as the dynamic process and activation energy. Especially, 20% Ti/3D g-C_3N_4 presents a high desulfurization rate, good desulfurization performance and cyclic stability in real diesel fuel. The work expands the application of Ti-based composite materials in the field of high-value catalytic conversion of diesel.

2. Experimental procedures

2.1. Chemicals and reagents

The detailed information is available in Supporting Information.

2.2. Characterization method

The detailed information is available in Supporting Information.

2.3. Catalyst preparation

2.3.1. Preparation of Ti/3D g-C_3N_4

The prepared TiO_2 precursor and three-dimensional porous g-C_3N_4 precursor (available in Supporting Information) are ground in the ratios of 1:9, 2:8 and 3:7. After the grinding and mixing, the precursor is spread flat in a covered crucible and placed in a tube furnace. Under the N_2 atmosphere protection, the precursor is then heated at a rate of 3 °C/min, rising from 25 to 550 °C, for 2 h. The catalyst materials are denoted as 10% Ti/3D g-C_3N_4, 20% Ti/3D g-C_3N_4 and 30% Ti/3D g-C_3N_4.

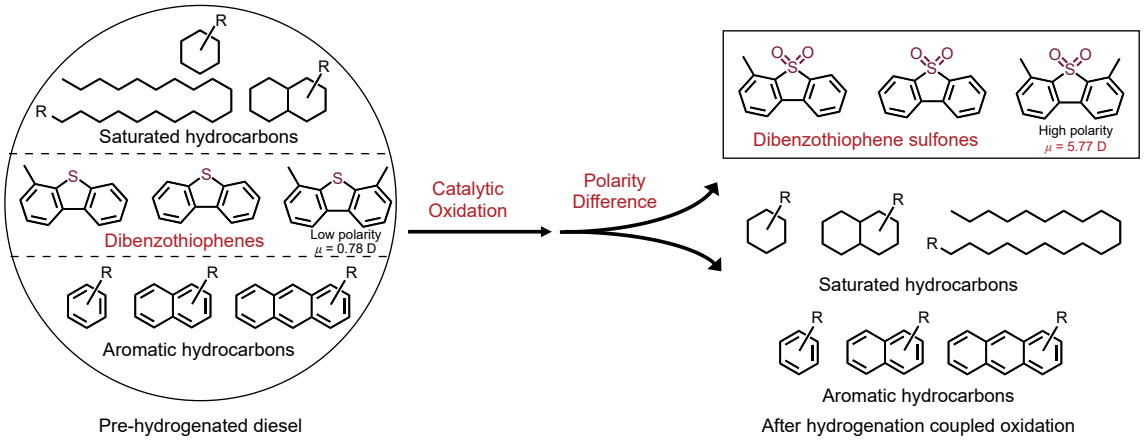

Scheme 1. High-value utilization of diesel components through catalytic oxidation.

2.3.2. Preparation of Ti/g-C_3N_4

The detailed informations are available in Supporting Information.

2.4. Oxidative desulfurization experiment

2.4.1. Steps of oxidative desulfurization of model oils

First, 50 mg of the selected catalyst is weighed in a customized 100 mL glass reactor with a condensation system. Then, 10 mL model oil (DBT, 4-MDBT and 4,6-DMDBT as substrates, 200 ppm S) is added, heated to the set temperature (from 40 to 60 °C) in a water bath. The magnetic stirring is carried out at the speed of 800 rpm, followed by the addition of a certain amount of H_2O_2 as an oxidant (different O/S ratio). According to different reaction conditions, 1 μL of the supernatant is measured with a micro-sampler at 10-min intervals, and the oil sample is injected into the gas chromatography for the determination and analysis of sulfur content.

2.4.2. Steps of oxidative desulfurization of real diesel

The detailed informations are available in Supporting Information.

ODS activity is calculated according to the following equation:

$$\text{ODS activity}\ (\%) = \frac{C_0 - C_t}{C_0} \times 100\% \quad (1)$$

C_0 refers to the sulfur concentration of the model oil or real oil before reaction (200 ppm for model oil and 704 ppm for real oil), C_t refers to the real-time sulfur concentration when taking samples at a fixed every 10 min.

2.4.3. Catalytic oxidation kinetics fitting and activation energy

The catalytic oxidation kinetics is fitted based on the data of the sulfur concentration at different times, according to the following equation:

$$\ln\frac{C_0}{C_t} = kt \quad (2)$$

The catalytic oxidation activation energy is obtained based the fitting of reaction temperature on the Arrhenius equation as follows:

$$k = Ae^{-\frac{E_a}{RT}} \quad (3)$$

2.5. Adsorbed performance tests

0.1 g of the selected adsorbent is weighed and added to a flask with 20 mL of model oil. Then, the flask is placed in a water bath at a stirring rate of 250 rpm. The adsorption process reaches adsorption saturation at 30 min. The oil samples are collected for analysis. The maximum adsorption capacity is calculated as follows:

$$q_t = \frac{(c_0 - c_t)\mathrm{V}}{m} \quad (4)$$

q_t refers to the adsorption capacity of the selected adsorbent in mg/g. C_0 is the sulfur concentration before adsorption (200 ppm), and C_t is the real-time sulfur concentration at 30 min.

3. Results and discussion

3.1. Characterization of catalysts

The images of TiO_2, 3D g-C_3N_4 and 20% Ti/3D g-C_3N_4 materials SEM are shown in Fig. 1(a)–(c). As the pure TiO_2 material appears as an irregular spherical shape, with a diameter of about 0.6–1.2 μm. The two-fold difference in diameter size is due to the close surface energy of metal oxides, which produces a bonding effect. Assembled by the lamellar porous structure and stacking in 3D space, the 3D g-C_3N_4 possesses a larger specific surface area, better pore structure and porosity than the traditional bulk carbon nitride. On the surface of 10% Ti/3D g-C_3N_4, the TiO_2 microspheres are distributed at a lower concentration (Fig. S1). Increasing the loading amount of TiO_2 to 20%, the distribution of the TiO_2 microspheres is enhanced, with an average diameter of the TiO_2 center of about 632 nm. Especially, the construction of heterostructures is intuitively observed in TEM images (Fig. 1(d) and (e)). Along the surface of TiO_2 microspheres, the mixed carbon nitride precursors undergo the in-situ heterostructure growth, resulting in a unique three-dimensional porous morphology. The heterojunction interface uniformly disperses at the edge position of 3D g-C_3N_4, mainly formed by the strong interaction between metal and carrier during the in-situ calcination process. Increasing TiO_2 loading to 30% results in partial agglomeration of metal oxide centers, which may lead to a decrease in the proportion of heterojunction interfaces. From the STEM mapping and EDX spectra of 20% Ti/3D g-C_3N_4, elements C, N, O and Ti can be found in Fig. 1(f)–(k) and Table S1. Importantly, the newly emerged heterostructure interface can become a high-performance ODS active center, due to the generation of the synergy effect. On one side of the heterostructure interface, porous materials promote adsorption, while on the other side, active Ti centers promote catalytic oxidation.

The heterostructure interface is determined by HRTEM and XRD in Fig. 2(a)–(c). The apparent lattices of anatase TiO_2 (101) and (004) crystal planes are confirmed along one side of the heterostructure interface. The statistical interplanar spacing of (101) is calculated to be about 0.352 nm (total 9 slices in 3.167 nm) in the IFFT simulation, resulting in the formation of the 25° peak signal in XRD. The crystal transformation of amorphous to anatase phase occurs, when the TiO_2 material is loaded onto 3D g-C_3N_4 through grinding and calcination, exposing the advantageous crystal surface of anatase (001), (004) and (200) planes. It is worth noting that the appearance of its heterojunction interface is accompanied by an increase in the crystalline strength of the (101) crystal plane. This indicates that controlling the directional growth of the crystal plane is beneficial for in-situ growth of g-C_3N_4. Along the other side of the heterostructure interface, the in-situ growth of carbon nitride lamellar structure can be observed. Correspondingly, the characteristic peaks near 13° and 28° are identified in the 3D g-C_3N_4 sample, respectively attributed to the (100) and (002) crystal planes of the carbon nitride, generated by in-plane stacking of conjugated aromatic rings. The diffraction peaks of the anatase TiO_2 are not readily apparent when the loading is 10%. Increasing the loading amount to 20%, the characteristic peak intensity of the anatase TiO_2 are enhanced. Together, the intensity decreases can also be observed in crystalline surfaces (100) and (002) of 3D g-C_3N_4, corresponding to the C–N triazine structural unit characteristic peak at 810 cm^{-1} in Fig. S2 FT-IR (Battula et al., 2024). Based on the electron microscopy and XRD analysis, more heterogeneous interfaces are generated during the in-situ growth of

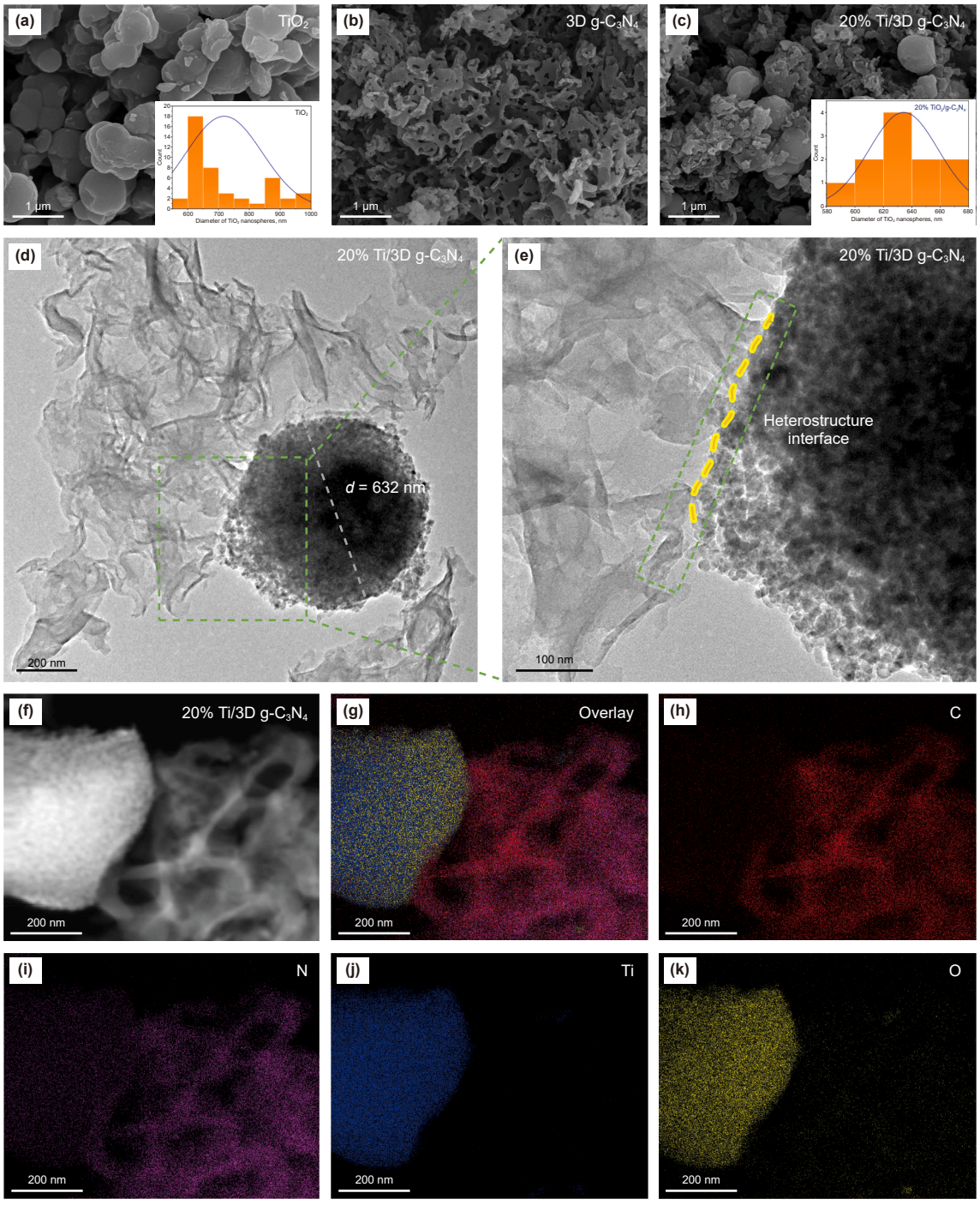

Fig. 1. Morphology characterization of prepared catalysts. (**a**) SEM image of TiO_2; (**b**) SEM image of 3D g-C_3N_4; (**c**) SEM image of 20% Ti/3D g-C_3N_4; (**d**) TEM image of 20% Ti/3D g-C_3N_4; (**e**) magnified TEM image of 20% Ti/3D g-C_3N_4; (**f**) STEM image of 20% Ti/3D g-C_3N_4; (**g**)–(**k**) EDX elemental mapping results of overlapped results, C, N, Ti and O, respectively. Inset in Fig. 1(a) and (c) are the TiO_2 particle size statistic results.

3D g-C_3N_4 onto the anatase TiO_2 surface. However, further increasing the TiO_2 loading amount to 30%, the aggregation of TiO_2 is inevitable. The results may cause a decrease in the proportion of exposed heterojunction interfaces, consistent with FT-IR analysis.

The UV spectra of the series of Ti/3D g-C_3N_4 materials are presented in Fig. 2(d). The UV absorption wavelength of pure TiO_2 is between 250 and 360 nm. When TiO_2 is loaded on the 3D g-C_3N_4 surface, the light response range of the composites is extended from the ultraviolet region to the ultraviolet-visible region. And the absorption around 350 nm is due to the introduction of the heterojunction interface, producing the electron excitation transitions from bonding orbitals to anti-bonding orbitals of hybrid materials (Zhong et al., 2018; Zou et al., 2018). According to the Tauc equation and in Fig. 2(e), the bandgap of the catalysts (E_g) can be obtained by calculation and simulation (Zhang et al., 2020). Compared to the bandgap of pure TiO_2 at 3.4 eV, the width of the Ti/3D g-C_3N_4 bandgap is narrowed to 2.9 eV. The blue shift indicates that the formation of the heterojunction interface

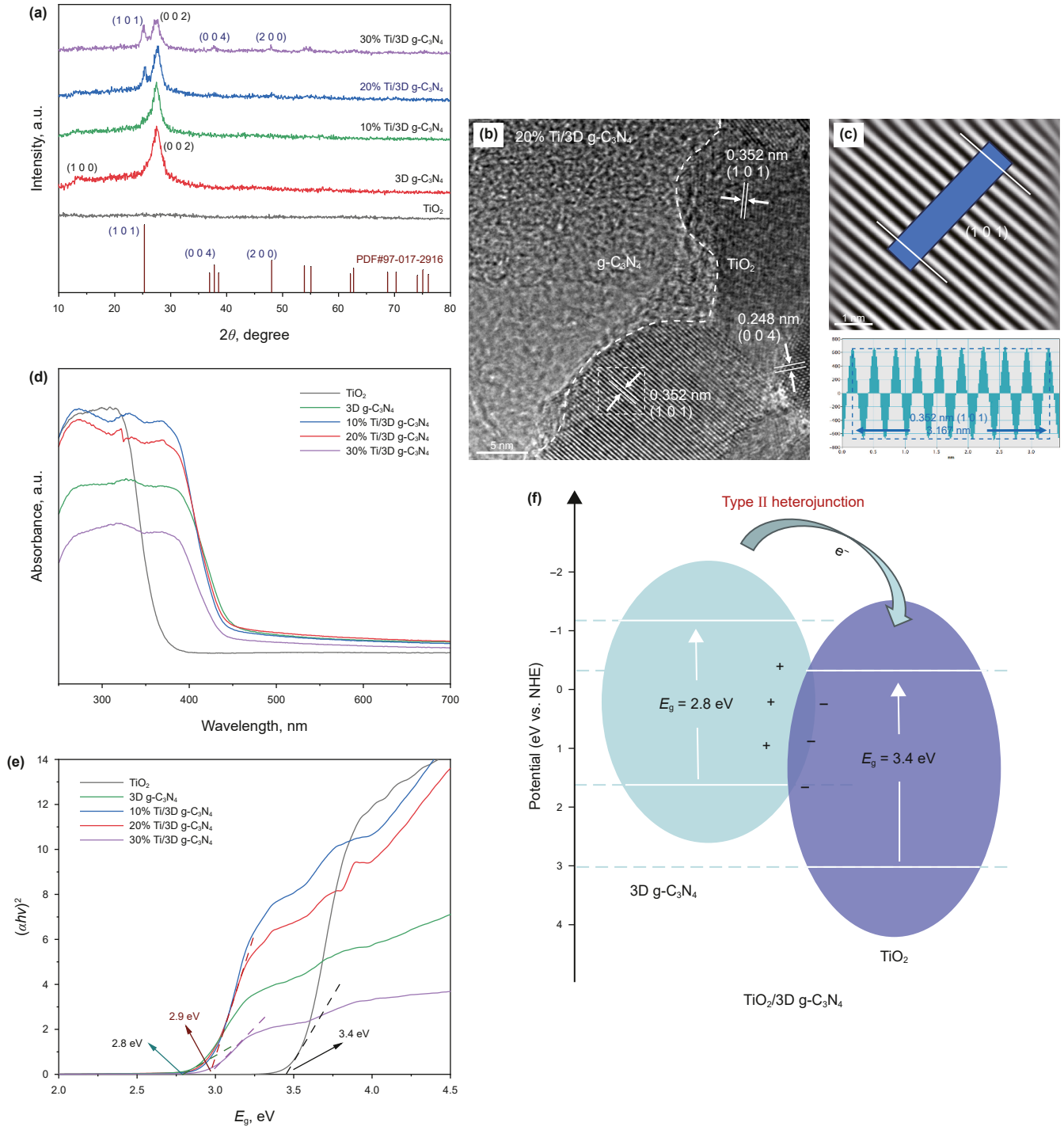

Fig. 2. Heterojunction structure characterization of prepared catalysts. (**a**) XRD pattern; (**b**) HRTEM image of heterostructure interface between anatase TiO_2 and 3D g-C_3N_4; (**c**) inverse fast Fourier transform (IFFT) of selected area and the corresponding average length statistics of (101) crystal plane in 20% Ti/3D g-C_3N_4; (**d**)–(**e**) UV-DRS and bandgaps of TiO_2, 3D g-C_3N_4, 10% Ti/3D g-C_3N_4, 20% Ti/3D g-C_3N_4, and 30% Ti/3D g-C_3N_4; (**f**) schematic diagram of the band structure of TiO_2 and 3D g-C_3N_4 forms a type II heterojunction.

effectively reduces the resistance of electronic conduction, as well as boosting the redox capability (Shi et al., 2025; Wang et al., 2014; Zhang et al., 2023).

As reported by Chen et al. (Chen et al., 2020; Wu et al., 2020; Zada et al., 2018), for the molecular orbital of the hybrid g-C_3N_4 materials, the valence band (VB) corresponds to the highest occupied molecular orbital (HOMO), while the conduction band (CB) corresponds to the lowest unoccupied molecular orbital (LUMO). Then, the empirical formulas are applied to calculate the CB and VB values of hybrid materials, as follows:

$$E_{CB} = X - E^e - 0.5E_g \quad (5)$$

$$E_{VB} = E_{CB} + E_g \quad (6)$$

where X represents the absolute electronegativity, E^e represents the free electrons on the hydrogen scale energy, and the E^e value is 4.5 eV.

The 3D g-C_3N_4, as an indirect bandgap semiconductor, has an X value of 4.73 eV, the E_{CB} (3D g-C_3N_4) value is calculated to

be −1.17 eV, and the E_{VB} (3D g-C_3N_4) value is calculated to be 1.63 eV. As for the TiO_2 metal oxides center, the *X* value is calculated to be 5.81 eV based on the parameters provided by Pearson (1988). E_{CB} (3D g-C_3N_4) and E_{VB} (3D g-C_3N_4) values are separately calculated to be −0.39 and 3.01 eV. The formation and the increased proportion of the type II heterojunction interfaces, between anatase TiO_2 and 3D g-C_3N_4, shortened the bandgap of the hybrid materials (Li et al., 2019). The mobility of thermally excited electrons from HOMO to LUMO levels is enhanced, facilitating the activation of low activity oxidants and substrate molecules in the ODS reaction (Chen et al., 2020).

The XPS spectra of the TiO_2/3D g-C_3N_4 materials are shown in Fig. 3. Four elements are detected in the survey of 20% Ti/3D g-C_3N_4. In the C 1s spectrum, the sp^2 hybrid carbon N–C=N signal of the aromatic ring structure is detected around 288.3 eV (Majdoub et al., 2020). Towards the direction of high binding energy in the N 1s spectrum, the characteristic signals of C–N–H and N–$(C)_3$ are respectively shifted by 0.2 and 0.4 eV, from 401.1 to 401.3 eV and from 399.6 to 400.0 eV (Xu et al., 2019). After the formation of the type II heterojunction interfaces of anatase TiO_2 and 3D g-C_3N_4, the N center at the edge and the backbone sites of the hybrid materials in a tendency to lose electrons. In the aromatic ring structure, the N element on the C–N=C signal of the sp^2 hybrid is in a stable state. Correspondingly, in the Ti 2p spectrum, the signals at 464.0 and 458.3 eV are attributed to Ti $2p_{1/2}$ and Ti $2p_{3/2}$ (Xiong et al., 2016). After the formation of the heterojunction, a 0.2 eV shift to the direction of low binding energy is observed, indicating a more electron-rich state for the Ti center of anatase TiO_2. In general, the construction of 20% Ti/3D g-C_3N_4 changes the charge density distribution: the N elements at the edge and backbone sites can transfer electrons to the metal Ti center after the formation of the heterojunction interfaces, consistent with the results discussed above.

The analysis of the N_2 adsorption-desorption isotherm and pore size distribution of the prepared TiO_2/3D g-C_3N_4 materials is shown in Fig. 4 and Fig. S3. The N_2 adsorption and desorption (cm^3/g) of the pure TiO_2 are at a low level, and its isotherm type belongs to type I isotherm with non-pore structure. The type IV adsorption curves and H3 type hysteresis loops are found, both in the 3D g-C_3N_4 and a series of Ti/3D g-C_3N_4 materials, indicating the presence of mesoporous and partial microporous structures. The N_2 adsorption capacity of the heterogeneous catalysts with different loading amounts showed a decreasing trend: 3D g-C_3N_4 > 10% Ti/3D g-C_3N_4 > 20% Ti/3D g-C_3N_4 > 30% Ti/3D g-C_3N_4. The corresponding pore structure parameters are presented in the pore size distribution of the supported catalyst (Table S2). The BET specific surface area of 3D g-C_3N_4 is 81.0 m^2/g, about 4 times that of the bulk g-C_3N_4 and 20% Ti/g-C_3N_4 (about 20 and 18 m^2/g). With the increase in TiO_2 loading, the specific surface area of the heterostructure catalysts decreases accordingly. In addition, from 3D g-C_3N_4 to 30% Ti/3D g-C_3N_4, the average pore size and pore volume are slightly reduced. Compared with pure TiO_2 and 20% Ti/g-C_3N_4, the formation of the heterostructure interface improves the dispersion of active Ti centers. And 3D g-C_3N_4 can maintain good

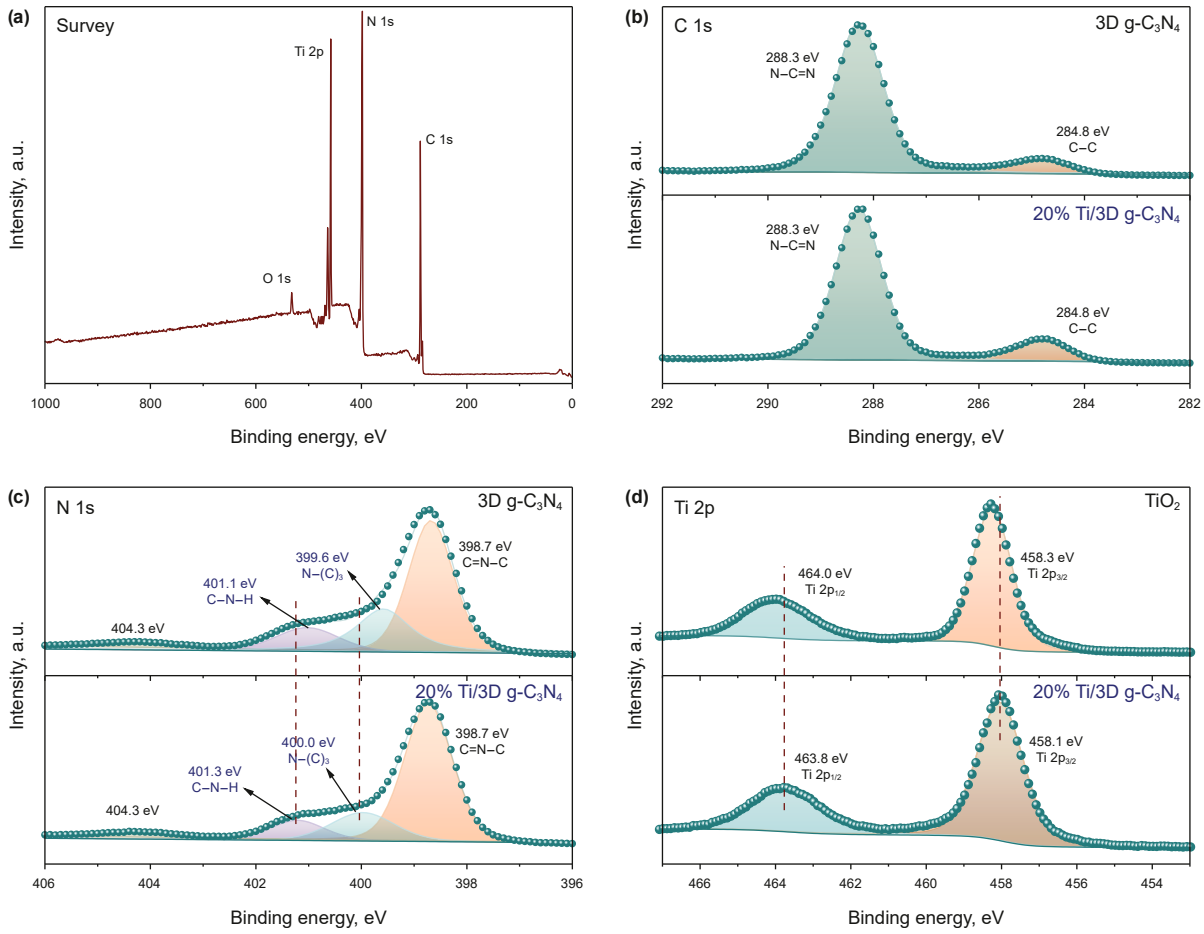

Fig. 3. Electronic structure and elemental states characterization of prepared catalysts. (**a**) XPS survey of all selected elements; (**b**)–(**d**) XPS elemental scanning of C 1s, N 1s and Ti 2p in 20% Ti/3D g-C_3N_4.

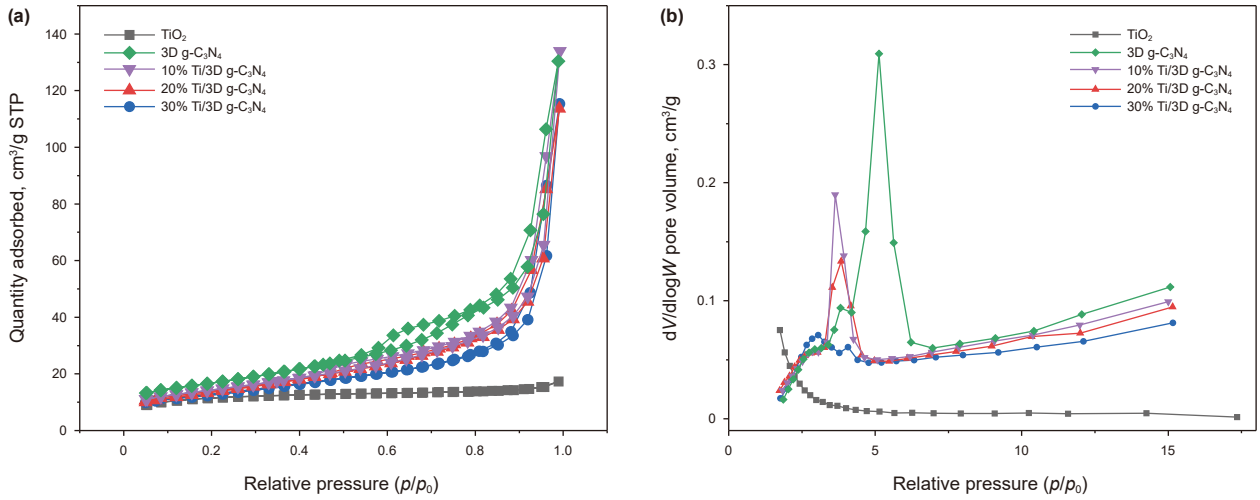

Fig. 4. Pore structure characterization of prepared catalysts. (**a**)–(**b**) Nitrogen adsorption-desorption isotherm and the corresponding pore size distribution results of TiO_2, 3D g-C_3N_4, 10% Ti/3D g-C_3N_4, 20% Ti/3D g-C_3N_4, and 30% Ti/3D g-C_3N_4.

microporous and mesoporous pores before and after the immobilization. The pore structure of 20% Ti/3D g-C_3N_4 is mainly mesoporous at about 4.5 nm, a small number of microporous junctions and some of macroporous structures, which makes the average pore size reach 5.0 nm and the pore volume reach 0.66 cm^3/g, strengthen the adsorption and mass transfer process of DBT sulfides (kinetic diameter <1 nm), and enhance their catalytic oxidation activity.

3.2. Performance evaluation of Ti/3D g-C_3N_4 heterojunction catalysts

To investigate the adsorption-promoted catalytic oxidative desulfurization of TiO_2/3D g-C_3N_4 materials, the static adsorption experiments towards DBT are conducted. As shown in Table 1, pure TiO_2 and g-C_3N_4 have almost no adsorption capacity, because of the restricted adsorption sites and adapted pore structure. After simple mixing using 20% Ti/g-C_3N_4, its maximum adsorption capacity slightly increased, possibly due to the presence of stacked pores and π-π interactions (Zhou et al., 2018). The adsorption capacity of 3D g-C_3N_4 reaches 9.1 mg S/g, which is due to the good transport and adsorption of DBT molecules (kinetic diameter <1 nm). The matching of molecular transport sizes promotes the reaction transfer of sulfides, in the mode of hierarchical pore for DBT molecular transfer in the three-dimensional stacking structure. When the TiO_2 is loaded onto the 3D g-C_3N_4 in increments, the heterostructure interface is formed. The adsorption capacity is in a tendency of first increasing and then decreasing. When introducing low-loading Ti centers onto a three-dimensional porous structure, an increased Ti loading can enhance its p-π adsorption of metal-sulfur interaction (Jin et al., 2016). And the π-π interaction also helps to promote the surface adsorption process, oriented by the effect between the triazine rings and the aromatic sulfides in the pore structure. Further excessively increasing the proportion of Ti leads to the aggregation of TiO_2, resulting in a decrease in the effective interface proportion, thus reducing the adsorption force and macroscopic adsorption capacity. In Figs. S4–S5, and Tables S3–S4, the 20% Ti/3D g-C_3N_4 material exhibits the maximum adsorption capacity of 14.4 mg S/g, promoting the quick enrichment of DBT on the surface of the catalyst by adsorption in the reaction. And the enhanced adsorption process conforms to the Langmuir model, and its kinetic process conforms to pseudo-second-order kinetics.

Table 1
Maximum adsorption capacity of TiO_2/3D g-C_3N_4 materials on DBT.

Entry	Sample	Adsorption capacity, mg S/g
1	TiO_2	0.4
2	g-C_3N_4	3.7
3	3D g-C_3N_4	9.1
4	10% Ti/g-C_3N_4	5.4
5	10% Ti/3D g-C_3N_4	12.5
6	20% Ti/3D g-C_3N_4	14.4
7	30% Ti/3D g-C_3N_4	13.8

The activity of catalytic oxidative desulfurization is conducted, and the results are shown in Fig. 5(a). Using pure TiO_2 material, 3D g-C_3N_4 and 20% Ti/g-C_3N_4 as the catalysts, the ODS rates are individually 22.7%, 16.3% and 49.7% within 80 min. When the heterojunction interface is formed between anatase TiO_2 and the 3D g-C_3N_4, the desulfurization rate is greatly increased. Especially, the maximum ODS rate of 99.7% can be obtained, where 20% Ti/3D g-C_3N_4 is used as the catalyst in the system. Overall, the adsorption of DBT in the first 10 min intensifies the ODS reaction process, accumulating DBT molecules in the π-π and p-π interactions. The resulting local high concentration of substrate promotes the acceleration of the ODS reaction rate. The ODS reaction rate decreases slightly with extended reaction time, which is caused by the lower concentration of the substrate and the self-decomposition of H_2O_2. Combined with the SEM and XRD, at 10% loading, the active TiO_2 center can be uniformly dispersed, but not saturated yet; Further increasing the loading amount to 30%, the effective proportion of heterojunction interfaces is reduced because of the crystal aggregation and swelling. Hence, the reactivity will be slightly reduced. Overall, the ODS performance is ranked as follows: 20% Ti/3D g-C_3N_4 > 30% Ti/3D g-C_3N_4 > 10% Ti/3D g-C_3N_4. The three-dimensional porous g-C_3N_4 can promote the directional adsorption of DBT, and the N element at the edge and skeleton of the material can transport electrons to the Ti center. And the reasonable proportion of heterogeneous structure interfaces enhances the synergistic effect of the ODS process. Herein, 20% Ti/3D g-C_3N_4 is chosen as the catalyst for the subsequent experiments.

To simulate the composition of the real catalytic hydrogenated diesel, different interfering components and reaction substrates

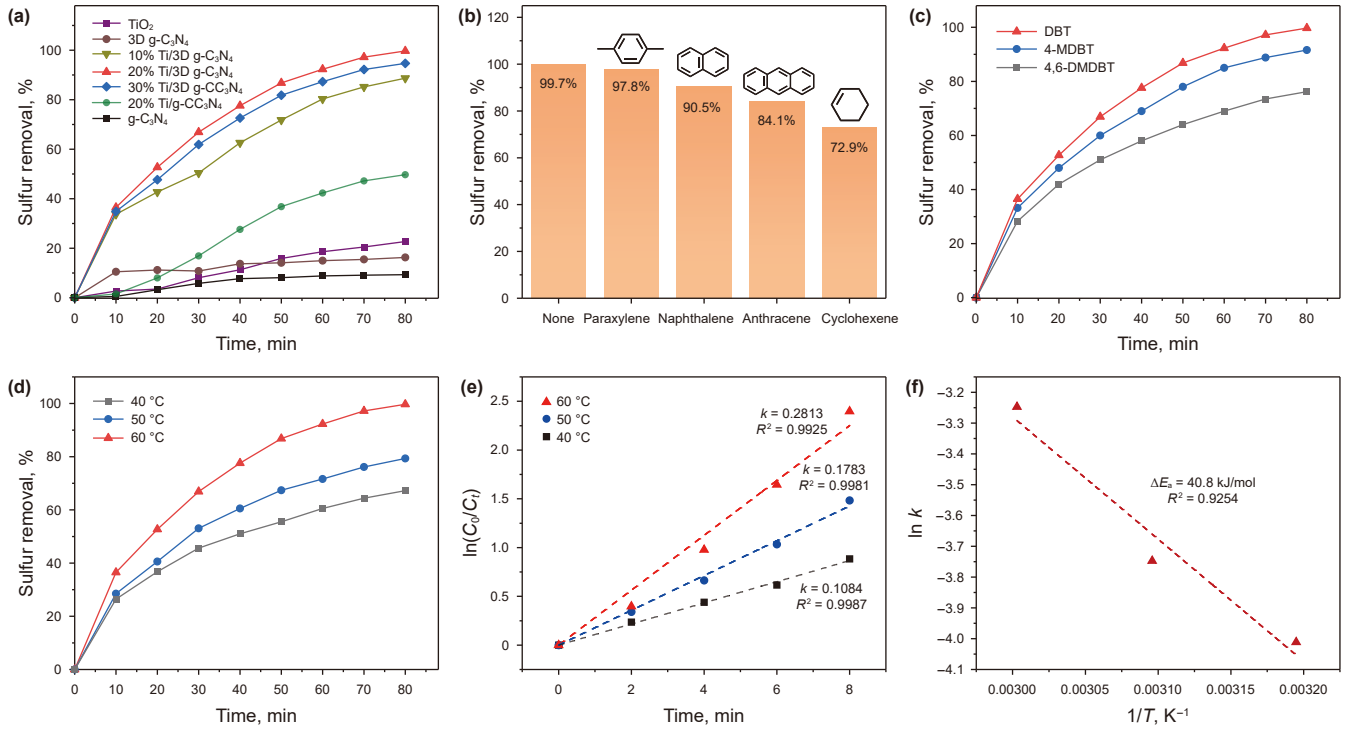

Fig. 5. Conditional experiment and the kinetic process of prepared catalysts. (**a**) Catalytic oxidative desulfurization activity with different catalyst systems; investigation of the impact of (**b**) different interferences; (**c**) different sulfur-containing substrates; (**d**) reaction temperatures on catalytic oxidative desulfurization activity; (**e**) fitting of the kinetic processes at different reaction temperatures and (**f**) fitting of the corresponding activation energy based on the Arrhenius equation.

are investigated in Fig. 5(b) and (c) and Fig. S6. DBT model oils containing 5 wt% paraxylene, naphthalene, anthracene, and cyclohexene are prepared to simulate the effects of interfering with aromatics, dicycloaromatic hydrocarbons, polycyclic aromatic hydrocarbons, and olefins. The cyclohexene exerts the most significant influence on the desulfurization rate, which may be attributed to the competitive oxidation between the C=C double bond and the DBT. The competitive oxidation reactions may lead to the oxidation of a small amount of cyclohexanones to cyclohexanothanol and cyclohexanonone (Wei et al., 2025). The ODS rate with cyclohexene attains only 72.9%. The impact of aromatic hydrocarbon disturbers, specifically naphthalene and anthracene, on ODS activity is found to be minimal at 90.5% and 84.1%, respectively. This is attributed to the increase in viscosity of the reaction system, which in turn affects the mass transfer and diffusion. The minimal impact of the paraxylene is found, with an activity of 97.8%. The results suggest that 20% Ti/3D g-C_3N_4 possesses effective anti-interference properties in ODS. Towards different aromatic sulfur substrates, the activity of the reaction is related to the steric hindrance. And the order of desulfurization rates is as follows: DBT (99.7%) > 4-MDBT (92.9%) > 4, 6-DMBT (78.6%).

The reaction temperature has a great influence on the ODS reaction, and the change in temperature will change the rate of reactive oxygen species formation. A reasonable increase in the reaction temperature is conducive to reaching the energy threshold of the ODS. As shown in Fig. 5(d), the activity of ODS increases rapidly in the first 10 min of the reaction, which is the contribution of the fast adsorption of DBT into the three-dimensional porous structure. The closer to the room temperature, the higher the adsorption capacity of 20% Ti/3D g-C_3N_4. Elevating the reaction temperature, the effective collision of molecules also increases, accelerating the generation rate of reactive oxygen species, which overpasses the reaction energy barrier. In general, the order of desulfurization temperature is as follows: 60 °C > 50 °C > 40 °C. And 60 °C is selected as the optimum reaction temperature. In addition, the kinetic process of the ODS reaction and the corresponding activation energy were successfully fitted in Fig. 5(e) and (f). Based on the fitting results of the matched pseudo-first-order kinetics and Arrhenius equation, the activation energy of the ODS reaction is approximately 40.8 kJ/mol. Above all, the prepared 20% Ti/3D g-C_3N_4 exhibited the optimal desulfurization rate, achieving 99.7% desulfurization within 80 min at a temperature of 60 °C, an O/S ratio of 4, and a catalyst dosage of 0.05 g (Fig. S7).

3.3. Proposed ODS mechanism

The mechanism of the reaction is elucidated through the free radical elimination assays, electron spin resonance (ESR), and gas chromatography-mass spectrometry (GC-MS). As demonstrated in Fig. 6(a) and (b), the ODS rate undergoes a substantial reduction when p-benzoquinone (BQ) is utilized as a radical eliminator. The reason can be explained as the $\cdot O_2^-$ radicals are preferentially captured by BQ, DBT substrates is lack of effective contact and activation with $\cdot O_2^-$, resulting in a decrease in the activity. In contrast, when dimethyl sulfoxide (DMSO) is employed as a trapper to capture hydroxyl radicals ·OH, no significant decrease in activity is observed, suggesting that ·OH is not the primary active species. Apart from that, the strong typical signal of PBN-$\cdot O_2^-$, the six-fold signal peak with the increasing reaction time, is detected through the ESR. An integral peak of GC around 6 min can be detected in the oil phase before the reaction (Fig. 6(c) and (d)). Based on the molecular ion peak information, mainly at 184 m/e in the mass spectrum, it can be determined that the substance is DBT. After the ODS process, the integral peak of DBT in the oil phase and the catalyst phase disappears. Instead, the only characteristic signal of $DBTO_2$ has been detected, around 10.3 min in the GC

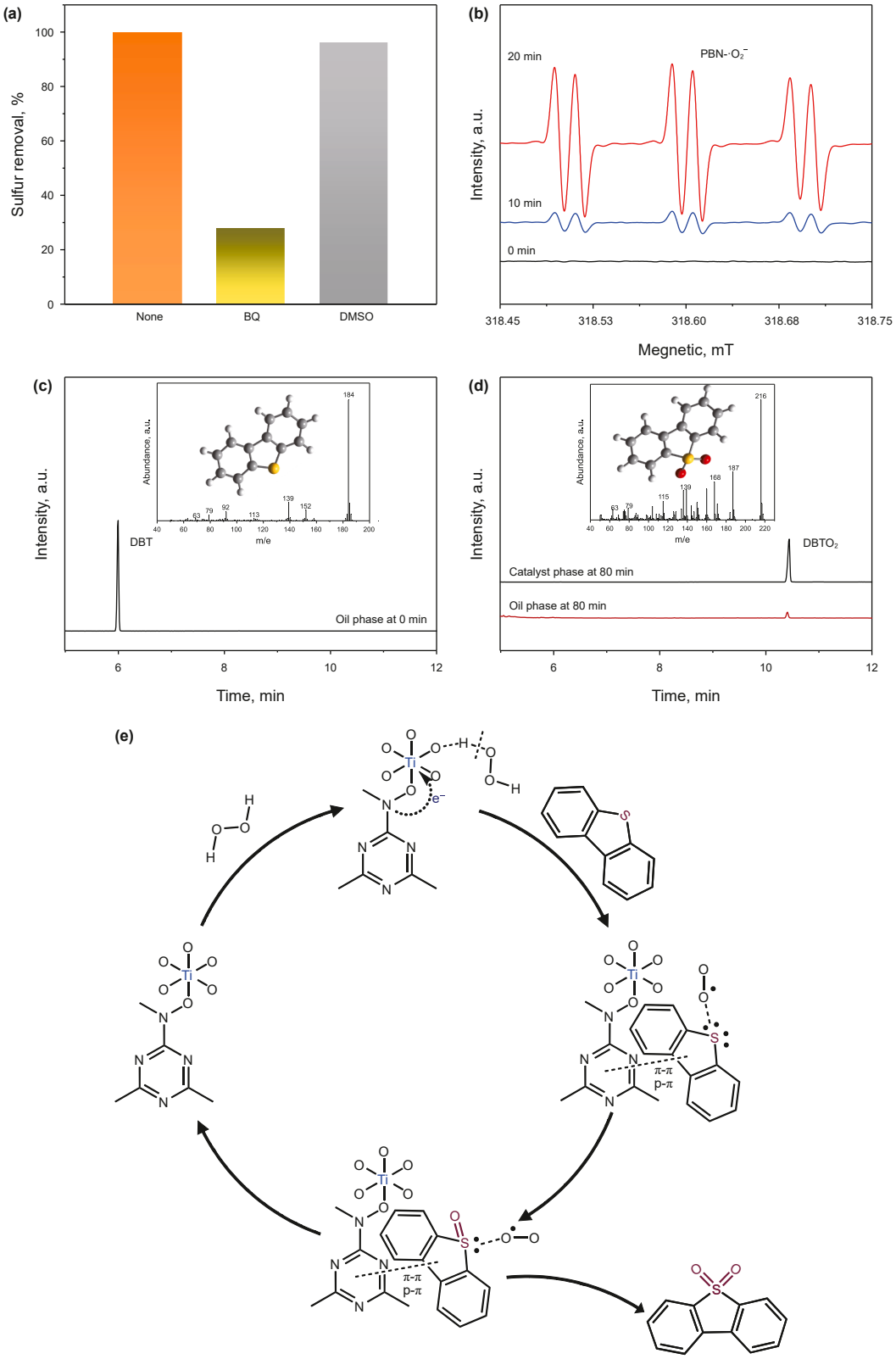

Fig. 6. Proposed reaction mechanism. (**a**) Free radical elimination experiments with dimethyl sulfoxide (DMSO) as a hydroxyl radical scavenger; benzoquinone (BQ) as a superoxide radical scavenger; (**b**) free radicals capture experiments using N-tert-Butyl-α-phenylnitrone (PBN) as the signal agent at different reaction times; GC-MS results of (**c**) the oil phase before reaction; (**d**) the oil phase and catalyst phase after reaction; (**e**) mechanism research of heterostructure TiO_2/3D g-C_3N_4 in ODS system.

spectrogram, at 216 m/e in the mass spectrum. It can be inferred that DBT is oxidized by $\cdot O_2^-$ to the only product $DBTO_2$. Based on the above characterization and conditional experiments, the possible reaction mechanism is proposed in Fig. 6(e).

When the heterojunction is formed in the Ti/3D g-C_3N_4 catalyst, the synergistic effect of adsorption-promoted catalytic oxidation occurs. At the onset of the reaction, the three-dimensional porous structure facilitates a directional adsorption towards the aromatic sulfide DBT. The effect arises from the mass transfer enhancement, of which the hierarchical pore for size matching effect, the metal-sulfur interaction for p-π effect, and the interaction of the triazine rings with the aromatic sulfides for π-π effect. The narrowed gap between the LUMO and HOMO levels contributes to the electron transfer, from the edge N and skeleton N sites of the carbon nitride towards the adjacent Ti center. The electron-rich Ti center can generate hydrogen bonds with H_2O_2 molecules in the form of Ti-O···H, where nucleophilic attack occurs (Chen et al., 2018). And the O–H bonds of hydrogen peroxide molecules can be broken, consequently forming the reactive $\cdot O_2^-$. Under the electric attack of $\cdot O_2^-$ towards electronic pairs on the S atom, DBT molecules can be converted into the intermediate products sulfoxide DBTO. Subsequently, the unstable DBTO is oxidized again by $\cdot O_2^-$, and the outcome is the formation of sulfone $DBTO_2$. The dipole moment of the substrate changes after the ODS, as the μ value of DBT is 0.78 D, and the μ value of $DBTO_2$ is 5.77 D (Li et al., 2016; Xu et al., 2015). Hence, the concentration of its substrate in the oil phase decreases, and the adsorption of sulfones on the catalyst surface increases, due to the presence of complexation and polarity difference.

3.4. Investigation of the hydrogenated diesel and the recycling performance

In the ODS desulfurization experiment of the hydrogenated diesel in Fig. 7(a). The initial sulfur content is measured at 704 ppm. After the first round of the ODS reaction, the residual sulfur content is determined to be 242 ppm, corresponding to 65.6% ODS rate. Immediately after the initial round of reaction, a separation of the oil phase and acetonitrile phase is conducted for a subsequent round of reaction. Following the second round of ODS reaction, the treated oil becomes more transparent. After the third round, the ODS rate reaches 98.7% with the remaining sulfur content of 9 ppm (less than 10 ppm, meeting the deep desulfurization standard), attaining the standard of deep desulfurization. And the cycling performances are also conducted in the model oil using 20% Ti/3D g-C_3N_4. Following seven cycles, the desulfurization rate is 95.7%, and the residual sulfur content is only 8.6 ppm (Fig. 7(b)). After alcohol washing the catalyst, its catalytic activity is enhanced. The analysis of XRD and FT-IR is shown in Fig. 7(c) and (d). The crystal structure of the catalyst surface remains

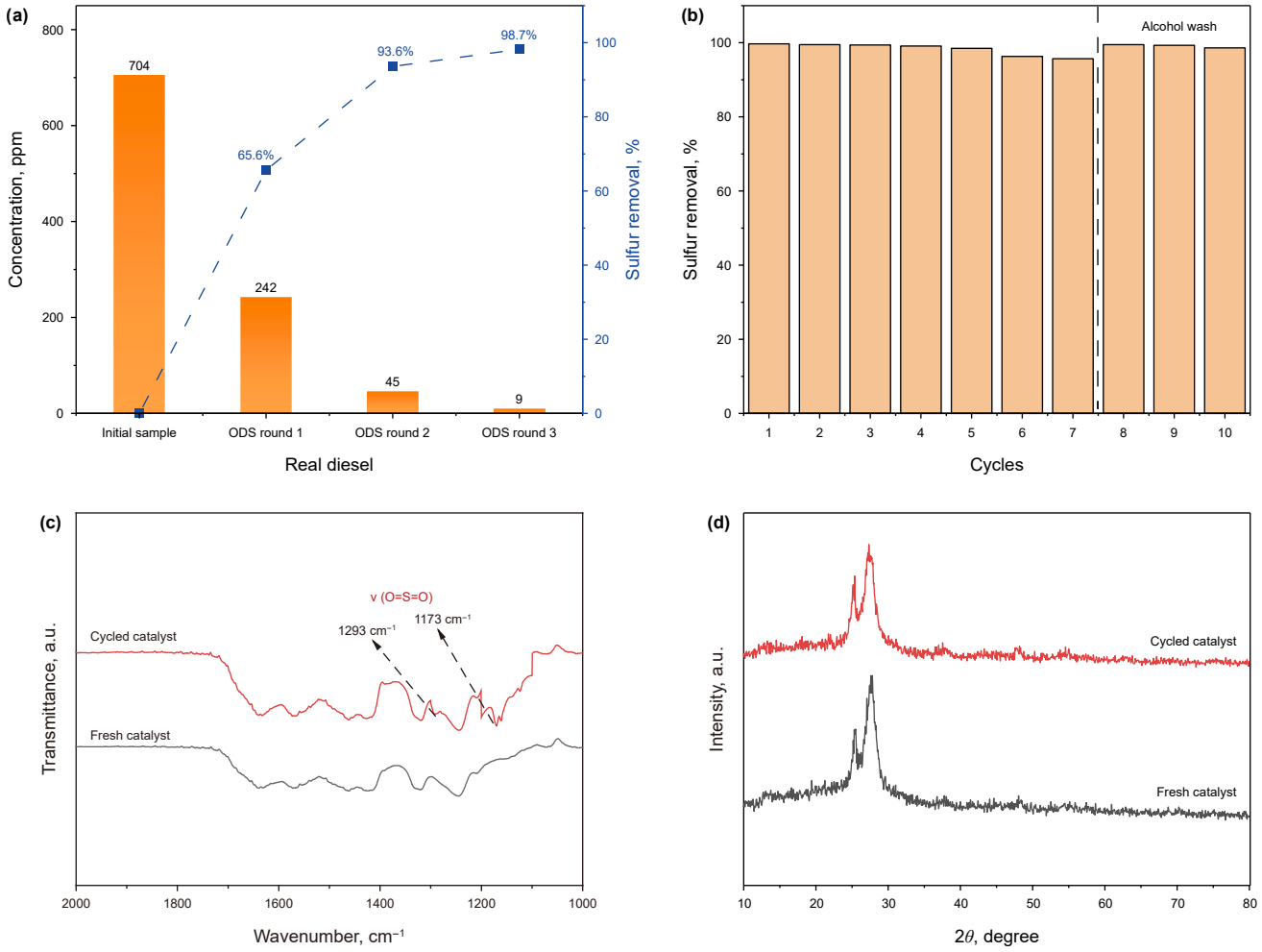

Fig. 7. Assessment of real oil and catalytic stability. (**a**) Multi-round catalytic oxidation performance of real diesel fuel, 704 ppm S; (**b**) the ODS cycle stability test using heterostructure TiO_2/3D g-C_3N_4 catalyst; (**c**) FT-IR and (**d**) XRD characterization of the catalyst after the ODS reaction.

unchanged before and after the reaction, demonstrating its stability. And the only characteristic signal of O=S=O is detected, corresponding to the sulfone products after the reaction (Fig. S8).

4. Conclusions

To conclude, towards the purpose of high-value utilization of the diesel components, a series of heterojunction Ti/3D g-C_3N_4 catalysts are prepared, then applied in the adsorption-promoted catalytic oxidation of the aromatic sulfides. The edge N(C–N–H) and skeleton N(N–$(C)_3$) groups within the carbon nitride exhibit electron-transport capabilities, facilitating the transfer of electrons to the Ti center. The optimization of the specific surface area and the pore structure is conducive to the mass transfer process. The synergistic effect between enhanced adsorption mass transfer and charge regulation is helpful for superoxide radical $\cdot O_2^-$ production. Accompanied by the process of free radicals, the aromatic sulfides are selectively oxidized into the corresponding sulfone substances, which are viewed as high-value products. The finding demonstrates the potential development of the bifunctional heterostructure catalysts and the high-value utilization of diesel fuel.

CRediT authorship contribution statement

Zhen-Dong Yu: Writing – original draft, Resources. **Peng Cui:** Writing – review & editing, Methodology. **Kai-Kai Li:** Data curation. **Su-Hang Xun:** Investigation. **Hao-Feng Wu:** Visualization. **Yi-Ru Zou:** Validation. **Xiao-Xiao Xing:** Formal analysis. **Xiao-Xiao Yu:** Software. **Pei-Wen Wu:** Conceptualization. **Wen-Shuai Zhu:** Supervision, Funding acquisition.

Declaration of interests

The authors declare that they have no known competing financial interests or personal relationships that could have appeared to influence the work reported in this paper.

Acknowledgments

All authors appreciate the financial support from Sinopec Research Institute of Petroleum Processing and the National Key R&D Program of China (No. 2022YFA1504403), National Science Foundation for Distinguished Young Scholars (No. 22425808), National Natural Science Foundation of China (Nos. U25D9013, 22178154, 22508420), Carbon Neutrality Research Institute Fund(CNIF20240103), Science Foundation of China University of Petroleum, Beijing (2462022YJRC002, 2462024XKBH002).

Supplementary Information

Supplementary Information to this article can be found online at https://doi.org/10.1016/j.petsci.2026.04.005.

References

Battula, V.R., Mark, G., Tashakory, A., et al., 2024. Binder-free carbon nitride panels for continuous-flow photocatalysis. ACS Catal. 14 (15), 11666–11674. https://doi.org/10.1021/acscatal.4c02349.

Chen, K., Zhang, X., Yang, X., et al., 2018. Electronic structure of heterojunction MoO_2/g-C_3N_4 catalyst for oxidative desulfurization. Appl. Catal. B Environ. Energy 238, 263–273. https://doi.org/10.1016/j.apcatb.2018.07.037.

Chen, H., Qiu, Y., Cai, Z., et al., 2025. Topological insulator heterojunction with electric dipole domain to boost polysulfide conversion in lithium-sulfur batteries. Angew. Chem. Int. Ed. 64 (13), e202423357. https://doi.org/10.1002/anie.202423357.

Chen, L., Ren, J., Yuan, Z., 2020. Atomic heterojunction-induced electron interaction in P-doped g-C_3N_4 nanosheets supported V-based nanocomposites for enhanced oxidative desulfurization. Chem. Eng. J. 387, 124164. https://doi.org/10.1016/j.cej.2020.124164.

Davis, S.J., Lewis, N.S., Shaner, M., et al., 2018. Net-zero emissions energy systems. Science 360 (6396). https://doi.org/10.1126/science.aas9793.

Dharmarajan, N.P., Vidyasagar, D., Yang, J.H., et al., 2023. Bio-inspired supramolecular self-assembled carbon nitride nanostructures for photocatalytic water splitting. Adv. Mater. 36 (2). https://doi.org/10.1002/adma.202306895.

He, J., Zhu, K., Jiang, W., et al., 2024. Synergistic catalysis of the N-hydroxyphthalimide on flower-like bimetallic metal-organic frameworks for boosting oxidative desulfurization. Petro. Sci. 21 (1), 674–682. https://doi.org/10.1016/j.petsci.2023.08.018.

Hu, C., Xun, S., Yang, B., et al., 2024. Heterostructure MoO_3/g-C_3N_4 efficient enhances oxidative desulfurization: rational designing for the simultaneously formation of MoO_3 nanoparticle and few layers g-C_3N_4. Sep. Purif. Technol. 340, 126789. https://doi.org/10.1016/j.seppur.2024.126789.

Hu, D., Wang, Q., Wang, X., et al., 2024. Experimental and mechanistic investigation of amide-based deep eutectic solvents for quinoline extraction and separation from wash oil. Ind. Eng. Chem. Res. 63 (12), 5397–5410. https://doi.org/10.1021/acs.iecr.3c04327.

Jin, T., An, S., Yang, X., et al., 2016. Efficient adsorptive desulfurization by task-specific porous organic polymers. AIChE J. 62 (5), 1740–1746. https://doi.org/10.1002/aic.15156.

Lazaar, N., Wu, S., Qin, S., et al., 2025. Single-atom catalysts on C_3N_4: minimizing single atom Pt loading for maximized photocatalytic hydrogen production efficiency. Angew. Chem. Int. Ed. 64 (6). https://doi.org/10.1002/anie.202416453.

Li, H., Zhu, W., Zhu, S., et al., 2016. The selectivity for sulfur removal from oils: an insight from conceptual density functional theory. AIChE J. 62 (6), 2087–2100. https://doi.org/10.1002/aic.15161.

Li, L., Li, L., Sun, T., et al., 2019. Novel $H_3PW_{12}O_{40}$/TiO_2-g-C_3N_4 type-II heterojunction photocatalyst with enhanced visible-light photocatalytic properties. J. Solid State Chem. 274, 152–161. https://doi.org/10.1016/j.jssc.2019.03.005.

Li, S., Wang, J., Cai, X., et al., 2026. From amorphous to ordered: ammonia-Mediated structural evolution in melon-based carbon nitride photocatalyst. Appl. Catal. B Environ. Energy 381, 125807. https://doi.org/10.1016/j.apcatb.2025.125807.

Liang, X., Zhang, T., Yu, H., et al., 2025. Control of dual-function amphiphilic biochar-MoO_{3-x} catalysts with abundant oxygen vacancies for efficient extractant-free oxidative desulfurization. Petro. Sci. 22 (5), 2215–2232. https://doi.org/10.1016/j.petsci.2025.02.021.

Liu, J., Liu, Y., Wang, Y., et al., 2025. Regulating the electron affinity of NiMo/Al_2O_3 to enhance ultra-deep hydrodesulfurization of diesel. Appl. Catal. B Environ. Energy 378, 125565. https://doi.org/10.1016/j.apcatb.2025.125565.

Liu, Q., Su, T., Zhang, H., et al., 2023. Development of TiO_2 catalyst based on Anderson-polyoxometalates for efficient visible-light-driven photocatalytic oxidative desulfurization. Fuel 333, 126286. https://doi.org/10.1016/j.fuel.2022.126286.

Liu, R., Deng, C., Chen, L., et al., 2025. Type III porous ionic liquids via lipophilicity differences for enhanced oxidation catalysis. AIChE J. 71 (5). https://doi.org/10.1002/aic.18751.

Ma, W., Ma, Y., Kong, L., et al., 2024. PW_{12}-MIL-101(Cr)/TiO_2 nanofibers: electrospinning synthesis and deep desulfurization performance under mild condition. Energy Fuels. 38 (7), 6325–6334. https://doi.org/10.1021/acs.energyfuels.4c00249.

Majdoub, M., Anfar, Z., Amedlous, A., 2020. Emerging chemical functionalization of g-C_3N_4: covalent/noncovalent modifications and applications. ACS Nano 14 (10), 12390–12469. https://doi.org/10.1021/acsnano.0c06116.

Pearson, R.G., 1988. Absolute electronegativity and hardness: application to inorganic chemistry. Inorg. Chem. 27, 734–740. https://doi.org/10.1021/ic00277a030.

Shi, Y., Zhao, R., Yang, W., et al., 2025. Interface-coupled supramolecular self-assembly 2D Z-scheme TiO_2/g-C_3N_4 heterojunction for efficient degradation of tetracycline under visible light. J. Alloys Compd. 1018, 179252. https://doi.org/10.1016/j.jallcom.2025.179252.

Tao, Y., Ding, J., Teng, Z., et al., 2025. Single-Pt-atom-decorated TiO_2 nanorod arrays for photoelectrochemical C–H chlorination. J. Am. Chem. Soc. 147 (22), 18814–18825. https://doi.org/10.1021/jacs.5c02551.

Vogt, E.T.C., Weckhuysen, B.M., 2024. The refinery of the future. Nature 629 (8011), 295–306. https://doi.org/10.1038/s41586-024-07322-2.

Wang, C., Zhu, W., Xu, Y., et al., 2014. Preparation of TiO_2/g-C_3N_4 composites and their application in photocatalytic oxidative desulfurization. Ceram. Int. 40 (8), 11627–11635. https://doi.org/10.1016/j.ceramint.2014.03.156.

Wang, Y., Hua, M., Zhou, S., et al., 2024. Regulating the coordination environment of surface alumina on NiMo/Al_2O_3 to enhance ultra-deep hydrodesulfurization of diesel. Appl. Catal. B Environ. Energy 357, 124265. https://doi.org/10.1016/j.apcatb.2024.124265.

Wei, X., Hong, Z., Fan, X., et al., 2025. Mechanistic study of cyclohexane oxidation to KA oil enabled by circulating microdroplets. Langmuir 41 (43), 29127–29135. https://doi.org/10.1021/acs.langmuir.5c03437.

Wu, P., Ma, S., Zhou, S., et al., 2025. Fe_3N nanoparticles confined in h-BN for ultra-deep oxidative desulfurization using molecular oxygen. Chem. Eng. Sci. 305, 121136. https://doi.org/10.1016/j.ces.2024.121136.

Wu, P., Song, X., Chen, L., et al., 2024. Few-layered hexagonal boron nitride nanosheets stabilized Pt NPs for oxidation promoted adsorptive desulfurization of fuel oil. Green Energy Environ. 9 (3), 495–506. https://doi.org/10.1016/j.gee.2022.08.003.

Wu, Z., Liang, Y., Yuan, X., et al., 2020. MXene Ti_3C_2 derived Z-scheme photocatalyst of graphene layers anchored TiO_2/g-C_3N_4 for visible light photocatalytic degradation of refractory organic pollutants. Chem. Eng. J. 394, 124921. https://doi.org/10.1016/j.cej.2020.124921.

Xia, R., Wang, W., Fu, Z., et al., 2025. Molecular characterization of waste tire pyrolysis oil: ^{14}C Distributidn and Potential por Sustainabls Fuels and fhemicals. Energy Fuels. 39 (17), 8107–8119. https://doi.org/10.1021/acs.energyfuels.5c00310.

Xiong, T., Cen, W., Zhang, Y., et al., 2016. Bridging the g-C_3N_4 interlayers for enhanced photocatalysis. ACS Catal. 6 (4), 2462–2472. https://doi.org/10.1021/acscatal.5b02922.

Xu, H., Han, Z., Zhang, D., et al., 2015. Theoretical elucidation of the dual role of [HMIm]BF_4 ionic liquid as catalyst and extractant in the oxidative desulfurization of dibenzothiophene. J. Mol. Catal. Chem. 398, 297–303. https://doi.org/10.1016/j.molcata.2014.12.018.

Xu, H., She, X., Fei, T., et al., 2019. Metal-oxide-mediated subtractive manufacturing of two-dimensional carbon nitride for high-efficiency and high-yield photocatalytic H_2 evolution. ACS Nano 13 (10), 11294–11302. https://doi.org/10.1021/acsnano.9b04443.

Ye, H., Zhou, M., Zeng, F., et al., 2025. Functional carbon materials with Lewis pairs for efficiently transforming sulfur compounds from waste to chemical. Appl. Catal. B Environ. Energy 374, 125399. https://doi.org/10.1016/j.apcatb.2025.125399.

Yoon, M., Park, Y., Sim, H., et al., 2025. 2D vacancy confinement in anatase TiO_2 for enhanced photocatalytic activities. Adv. Mater. 37 (15). https://doi.org/10.1002/adma.202413062.

Yu, Z., Wang, D., Xun, S., et al., 2018. Amorphous TiO_2-supported Keggin-type ionic liquid catalyst catalytic oxidation of dibenzothiophene in diesel. Pretro. Sci. 15 (4), 870–881. https://doi.org/10.1007/s12182-018-0268-4.

Yu, Z., Xun, S., Jing, M., et al., 2022. Construction of 3D TiO_2 nanoflower for deep catalytic oxidative desulfurization in diesel: role of oxygen vacancy and Ti^{3+}. J. Hazard. Mater. 440, 129859. https://doi.org/10.1016/j.jhazmat.2022.129859.

Zada, A., Qu, Y., Ali, S., et al., 2018. Improved visible-light activities for degrading pollutants on TiO_2/g-C_3N_4 nanocomposites by decorating SPR Au nanoparticles and 2,4-dichlorophenol decomposition path. J. Hazard. Mater. 342, 715–723. https://doi.org/10.1016/j.jhazmat.2017.09.005.

Zeng, F., Feng, Y., Wang, J., et al., 2025. Insight into the structure-dependent effects of metal residues in conjugated polymers. Chem. Commun. 61 (53), 9626–9629. https://doi.org/10.1039/d5cc01594d.

Zhang, Y., Di, J., Zhu, X., et al., 2023. Chemical bonding interface in $Bi_2Sn_2O_7$/BiOBr S-scheme heterojunction triggering efficient N_2 photofixation. Appl. Catal. B Environ. Energy 323, 122148. https://doi.org/10.1016/j.apcatb.2022.122148.

Zhang, Y., Xu, J., Mei, J., et al., 2020. Strongly interfacial-coupled 2D-2D TiO_2/g-C_3N_4 heterostructure for enhanced visible-light induced synthesis and conversion. J. Hazard. Mater. 394, 122529. https://doi.org/10.1016/j.jhazmat.2020.122529.

Zheng, P., Zhu, Z., Xiao, C., et al., 2025. Insight into oxidative desulfurization mechanism from the interaction between different facets of TiO_2 and V single atom or V_2O_5 cluster. Inorg. Chem. 64 (18), 8885–8894. https://doi.org/10.1021/acs.inorgchem.4c05395.

Zhong, R., Zhang, Z., Yi, H., et al., 2018. Covalently bonded 2D/2D O-g-C_3N_4/TiO_2 heterojunction for enhanced visible-light photocatalytic hydrogen evolution. Appl. Catal. B Environ. Energy 237, 1130–1138. https://doi.org/10.1016/j.apcatb.2017.12.066.

Zhou, N., Huang, X., Zhang, Y., et al., 2018. High performances of mesoporous g-C_3N_4 for adsorptive desulfurization in model gasoline (iso-octane) solutions. Appl. Surf. Sci. 448, 636–641. https://doi.org/10.1016/j.apsusc.2018.04.084.

Zou, Y., Yang, B., Liu, Y., et al., 2018. Controllable interface-induced Co-assembly toward highly ordered mesoporous Pt@TiO_2/g-C_3N_4 heterojunctions with enhanced photocatalytic performance. Adv. Funct. Mater. 28 (50). https://doi.org/10.1002/adfm.201806214.